

# Nonlinear evolution of the firehose instability in a magnetic dipole geotail geometry<sup>a)</sup>

H. Vernon Wong,<sup>b)</sup> B.-Y. Xu, W. Horton, J. Pratt, and J. W. Van Dam  
*Institute for Fusion Studies, University of Texas, Austin, Robert Lee Moore Hall, Austin,  
 Texas 78712-1060*

(Received 18 November 2004; accepted 15 February 2005; published online 5 May 2005)

Bursty bulk flows increase the parallel pressure faster than the perpendicular pressure in the high- $\beta$  central plasma sheet driving the firehose instability [S. Ji and R. A. Wolf, *J. Geophys. Res.* **108**, 1191 (2003); **30**, 2242 (2003)]. A nonlinear partial differential equation is derived and an initial-value code developed to investigate the firehose anisotropy-driven turbulence in the Earth's geotail. It is essential to include dispersive ion kinetic effects in order to limit the range of linearly unstable parallel wave numbers and to achieve a stationary nonlinear turbulent state. The nonlinear dynamics of the firehose instability provides a possible explanation for ultralow-frequency Pi-2 fluctuations associated with bursty bulk flows and substorms. © 2005 American Institute of Physics. [DOI: 10.1063/1.1888786]

## I. INTRODUCTION

In the plasma sheet of the Earth's geomagnetic tail, plasma flows which transport mass, energy, and magnetic flux earthward appear to be highly variable rather than steady. These intermittent and variable flows are particularly prevalent during periods of substorm activity (arising from the distortions of the Earth's magnetosphere by periods of southward pointing interplanetary magnetic fields and enhanced solar wind velocities), and they are referred to as "bursty bulk flows" (BBFs).

Chen and Wolf<sup>1</sup> have proposed that these BBFs are due to the formation and earthward acceleration of underpopulated flux tubes called "bubbles." A likely mechanism for the creation of such bubbles is magnetic reconnection across the thin current sheet separating the northern and southern lobes of the Earth's geotail. The plasma pressure inside a bubble is initially lower than that of neighboring flux tubes, but the magnetic field is higher in order that the perpendicular gradient of the total (magnetic plus plasma) pressure be the same as in the surrounding medium. The stronger magnetic tension force of the curved field lines inside the bubble is no longer in balance with the perpendicular gradient of the total pressure, and the bubble is accelerated earthwards. Chen and Wolf used the magnetohydrodynamic (MHD) equations for plasmas with isotropic pressure to numerically simulate the dynamics of a bubble moving through a two-dimensional (2D) equilibrium plasma model of the Earth's geomagnetic tail. The characteristics of the simulated bubble seem to be qualitatively consistent with most of the measured properties of BBFs.

Ji and Wolf<sup>2,3</sup> repeated the bubble simulation of Chen and Wolf using the anisotropic MHD equations of Chew, Goldberger, and Low (CGL).<sup>4</sup> Turbulent magnetic perturbations were observed propagating parallel to the magnetic

field. Due to the rapid shortening of the flux tube length as the bubble propagates earthward, pressure anisotropy with the parallel plasma pressure greater than the perpendicular pressure ( $P_{\parallel} > P_{\perp}$ ) is created and maintained by the Fermi acceleration mechanism as particles are forced to reflect over shorter and shorter path lengths along the field line. Growth of magnetic perturbations was attributed to the firehose instability, with linear growth rates proportional to the parallel wave number as predicted by the linearized CGL equations. However, it is not possible to follow the time evolution of the instabilities into the nonlinear regime due to dominance of short wavelength modes of the order of grid scale lengths. This breakdown is due to the exclusion of dispersive kinetic effects in their numerical simulation. Dispersive kinetic effects limit the domain of unstable parallel wave numbers for the firehose instability, and this dispersion will strongly affect the evolution of the instability into the nonlinear regime.

In this work, we discuss the nonlinear evolution of firehose instabilities in a mirror geometry with the inclusion of dispersive effects. We do not attempt to simulate the motion of a filament of flux tubes through a background medium. Instead, we focus on the derivation and simulation of a nonlinear partial differential equation for the firehose instability which enables us to predict a nonlinear spectrum of magnetic perturbations generated by firehose instabilities. We investigate the possibility that firehose instabilities may be responsible for the irregular bursts of ultralow-frequency electromagnetic waves called Pi-2 pulsations in the 2–25 mHz band. The Pi-2 pulsations are observed in the geomagnetic tail during the substorm growth phase, a period characterized by enhanced plasma convection and bursty bulk flows.<sup>5–7</sup>

In Sec. II, we discuss the kinetic dispersion relation for the low-frequency right-hand circularly polarized electromagnetic wave propagating in a uniform plasma parallel to the equilibrium homogeneous magnetic field. We derive the local fluid limit of the firehose dispersion relation with the inclusion of dispersive effects in the limit of small tempera-

<sup>a)</sup>Paper RI2 5, *Bull. Am. Phys. Soc.* **49**, 327 (2004).

<sup>b)</sup>Invited speaker.

ture anisotropy. In Sec. III, we derive the nonlinear partial differential equation for the firehose instability in a mirror geometry, starting from the Chew–Goldberger–Low equations for a plasma with anisotropic pressure. In numerical simulations of plasma instabilities, it is necessary to dissipate the energy at short wavelengths with scale lengths of the order of grid dimensions, and in Sec. IV we discuss the modifications of the nonlinear firehose partial differential equation introduced by plasma resistivity, plasma viscosity, and plasma dispersive effects. In Sec. V we discuss the numerical simulations. We describe the numerical method and we present results for three different types of Alfvén turbulence driven by the firehose instability in a mirror geometry modeling the Earth’s geotail. We find that the nonlinear firehose-driven fluctuations have a rich frequency and parallel wavelength spectrum and that the value of the local nonlinear firehose stability parameter  $\sigma(t)$  fluctuates, with short-lived excursions into the unstable domain  $\sigma(t) < 0$ . In Sec. VI, we compare the substorm-associated Pi-2 fluctuations and the turbulent fluctuations generated by the numerical calculations. In Sec. VII, we summarize our conclusions.

## II. LINEAR DISPERSION RELATION

In this section, we discuss the firehose dispersion relation for parallel propagation in a uniform magnetic field. We consider the equilibrium magnetic field  $\mathbf{B}_0 = B_0 \hat{\mathbf{z}}$  to be in the  $z$  direction and the equilibrium distribution function  $F_0$  to be bi-Maxwellian:

$$F_0 = N_0 \frac{m}{2\pi T_\perp} \left( \frac{m}{2\pi T_\parallel} \right)^{1/2} e^{-mv_\parallel^2/2T_\parallel} e^{-mv_\perp^2/2T_\perp},$$

with equilibrium density  $N_0$ , parallel temperature  $T_\parallel$ , and perpendicular temperature  $T_\perp$ .

The perturbed electromagnetic fields,  $\delta\mathbf{E}$  and  $\delta\mathbf{B}$ , are taken to be of the form

$$\delta\mathbf{E} = \delta\mathbf{E} \exp(ik_\parallel z - i\omega t) + \text{c.c.};$$

$\delta\mathbf{B} = \delta\mathbf{B} \exp(ik_\parallel z - i\omega t) + \text{c.c.}$ , with  $\delta\mathbf{E}$  and  $\delta\mathbf{B}$  perpendicular to  $\mathbf{B}_0$ ,  $\delta\mathbf{B} = k_\parallel c / \omega \mathbf{z} \times \delta\mathbf{E}$ , where  $\omega$  is the mode frequency and  $k_\parallel$  the parallel wave number.

Parallel propagating electromagnetic waves can be separated into right- and left-hand circularly polarized waves. The dispersion relation for the right-hand circularly polarized wave is given by Stix<sup>8</sup> and Gary:<sup>9</sup>

$$\frac{k_\parallel^2 c^2}{\omega^2} = 1 - \sum \frac{\omega_p^2}{\omega^2} \left\{ \left( 1 - \frac{T_\perp}{T_\parallel} \right) [1 + \alpha Z(\alpha)] - \frac{\omega}{k_\parallel} \left( \frac{m}{2T_\parallel} \right)^{1/2} Z(\alpha) \right\}, \quad (1)$$

where the summation is over ions and electrons. For the ions, we have  $\alpha = (\omega + \Omega_i) / k_\parallel v_i$  and for the electrons we have  $\alpha = (\omega - |\Omega_e|) / k_\parallel v_e$ . The ion and electron thermal velocities are defined by  $v_i = (2T_\parallel / m_i)^{1/2}$  and  $v_e = (2T_e / m_e)^{1/2}$ , and the plasma dispersion function  $Z(\alpha)$  is defined by

$$Z(\alpha) = \left( \frac{1}{\pi} \right)^{1/2} \int_{-\infty}^{\infty} d\xi \frac{\exp(-\xi^2)}{\xi - \alpha}, \quad (2)$$

with  $\text{Im}(\alpha) > 0$ .

Assuming isotropic cold electrons with  $T_{\parallel e} = T_{\perp e} = T_e$ ,  $\omega \ll |\Omega_e|$ , and  $|\alpha_e| \gg 1$ , we have

$$\frac{\omega_{pe}^2}{\omega k_\parallel v_e} Z(\alpha_e) = - \frac{\omega_{pe}^2}{\omega(\omega - |\Omega_e|)} \sim \frac{\omega_{pe}^2}{\omega |\Omega_e|} = \frac{\omega_{pi}^2}{\omega \Omega_i},$$

and the dispersion relation can be written as follows:

$$\frac{\omega^2 v_i^2}{\Omega_i^2 c^2} - k_\parallel^2 \rho_i^2 + \beta_{\parallel i} \left( \frac{\omega}{\Omega_i} - 1 + \frac{T_{\perp i}}{T_{\parallel i}} \right) - \frac{\beta_{\parallel i}}{k_\parallel \rho_i} \left\{ 1 - \frac{T_{\perp i}}{T_{\parallel i}} \left( 1 + \frac{\omega}{\Omega_i} \right) \right\} Z(\alpha_i) = 0, \quad (3)$$

where  $\rho_i = v_i / \Omega_i$  and  $\beta_{\parallel i} = 8\pi N_0 T_{\parallel i} / B_0^2$ .

This dispersion relation predicts instability for temperature anisotropy of either sign,  $[(T_{\parallel i} / T_{\perp i}) - 1]^2 \neq 0$ . From a Nyquist analysis of the dispersion relation, we obtain the following instability criterion which places an upper limit on the magnitude of  $k_\parallel$ :

$$\left( \frac{v_i^2}{c^2} + \frac{\beta_{\parallel i} T_{\perp i}}{T_{\parallel i}} \right) \left( \frac{T_{\parallel i}}{T_{\perp i}} - 1 \right)^2 > k_\parallel^2 \rho_i^2. \quad (4)$$

Typically  $v_i^2 / c^2 \ll 1 \leq \beta_{\parallel i} T_{\perp i} / T_{\parallel i}$ , and we will ignore terms proportional to  $v_i^2 / c^2$ .

In the case of small temperature anisotropy and modest values of plasma  $\beta$ , where  $1 > (\beta_{\parallel i} T_{\perp i} / T_{\parallel i}) [(T_{\parallel i} / T_{\perp i}) - 1] > (\beta_{\parallel i} T_{\perp i} / T_{\parallel i}) [(T_{\parallel i} / T_{\perp i}) - 1]^2$ , the unstable parallel wave numbers are small  $k_\parallel^2 \rho_i^2 < 1$ . The instability is due to resonant particle interactions, and the unstable growth rate  $\gamma$  is small, with  $\gamma \ll \omega$ .

However, in the case of small anisotropy  $1 > [(T_{\parallel i} / T_{\perp i}) - 1] > 0$  with the parallel temperature  $T_{\parallel i}$  exceeding the perpendicular temperature  $T_{\perp i}$ , and large plasma beta  $\beta$ ,  $\beta_{\parallel i} T_{\perp i} / 2T_{\parallel i} [(T_{\parallel i} / T_{\perp i}) - 1] > 1$ , the character of the instability is transformed from a resonant particle instability into a fluidlike instability involving the velocity moments of the equilibrium distribution function. The dispersion relation given by Eq. (3) can then, in the limit of  $\omega / \Omega_i < 1$  and  $k_\parallel \rho_i < 1$ , be approximated by

$$\omega^2 - \frac{\omega}{\Omega_i} k_\parallel^2 V_A^2 \left[ 1 + \frac{\beta_{\parallel i}}{2} \left( 2 - \frac{T_{\perp i}}{T_{\parallel i}} \right) \right] + \frac{k_\parallel^2 V_A^2 \beta_{\parallel i}}{2} \left( 1 - \frac{T_{\perp i}}{T_{\parallel i}} - \frac{2}{\beta_{\parallel i}} \right) = 0, \quad (5)$$

where the function  $Z(\alpha)$  in Eq. (3) is replaced by its large argument asymptotic expansion  $Z(\alpha) \rightarrow -(1/\alpha) - [1/(2\alpha^3)] - \dots$ . This is the dispersion relation for the unstable firehose mode, unstable when  $[1 - (T_{\perp i} / T_{\parallel i}) - (2/\beta_{\parallel i})] > 0$ . In this domain of parameter space, the instability is fluidlike in character.

Note that, in Eq. (5), the linear dispersive term in  $\omega$  is ignorable for small wave numbers where  $k_\parallel \rho_i \sim |\omega / \Omega_i| \ll 1$ , and the growth rate is proportional to  $k_\parallel$ . However, at larger

wave numbers where  $k_{\parallel}\rho_i \sim |\omega/\Omega_i|^{1/2} < 1$ , this dispersive term is no longer ignorable and the growth rate attains its maximum value.

The maximum growth rate is given by

$$\frac{\omega_0}{\Omega_i} = (1+i) \left( 1 - \frac{T_{\perp i}}{T_{\parallel i}} - \frac{2}{\beta_{\parallel i}} \right) \left/ \left( 2 - \frac{T_{\perp i}}{T_{\parallel i}} + \frac{2}{\beta_{\parallel i}} \right) \right.$$

at wave number  $k_{\parallel 0}$ , where

$$k_{\parallel 0}\rho_i = 2 \left( 1 - \frac{T_{\perp i}}{T_{\parallel i}} - \frac{2}{\beta_{\parallel i}} \right)^{1/2} \left/ \left( 2 - \frac{T_{\perp i}}{T_{\parallel i}} + \frac{2}{\beta_{\parallel i}} \right) \right.$$

Mode damping due to ion wave-particle resonance is exponentially small except at large parallel wave numbers with  $k_{\parallel}\rho_i \sim 1$ . Wave-particle resonances lead to progressively larger velocity space gradients in the particle distribution function, gradients which are eventually limited by particle collisions and microscale turbulence. In numerical investigations of ion-acoustic waves and the ion temperature gradient instability, ion Landau damping is represented by an integral operator. This nonlocal damping occurs throughout the  $k_{\parallel}$  spectrum and represents a dissipative closure of the divergence of the parallel thermal flux. In the numerical simulations presented here, it will suffice to dissipate the energy in short wavelength fluctuations ( $k_{\parallel}\rho_i > 1$ ) of the order of “grid” scale lengths by the introduction of plasma resistivity and viscosity, modeled by differential operators (see Sec. IV)

### III. ANISOTROPIC MHD MODE IN MIRROR GEOMETRY

In this section, we discuss the derivation of a nonlinear partial differential equation for the firehose mode in a two-dimensional (2D) high-pressure plasma equilibrium model of the Earth’s geotail.

The starting point is the hydromagnetic fluid equation of (CGL),

$$\rho \left( \frac{\partial \mathbf{v}}{\partial t} + \mathbf{v} \cdot \nabla \mathbf{v} \right) = -\nabla \cdot \mathbf{P} + \frac{1}{c} \mathbf{J} \times \mathbf{B}. \quad (6)$$

The plasma pressure  $\mathbf{P}$  is a dyadic given by  $\mathbf{P} = P_{\perp}(\mathbf{I} - \mathbf{b}\mathbf{b}) + P_{\parallel}\mathbf{b}\mathbf{b}$ , where  $\mathbf{I}$  is the unit dyadic,  $\mathbf{b}$  is the unit vector in the direction of the magnetic field  $\mathbf{B}$ , and  $P_{\perp}$  and  $P_{\parallel}$  are the perpendicular and parallel pressure components, respectively.

Note that

$$\nabla \cdot \mathbf{P} = \nabla P_{\perp} + \mathbf{B}\mathbf{B} \cdot \nabla \left( \frac{P_{\parallel} - P_{\perp}}{B^2} \right) + \frac{(P_{\parallel} - P_{\perp})}{B^2} \mathbf{B} \cdot \nabla \mathbf{B}$$

and that

$$\begin{aligned} \nabla \cdot \mathbf{P} - \frac{1}{c} \mathbf{J} \times \mathbf{B} &= \nabla P_{\perp} + \mathbf{B}\mathbf{B} \cdot \nabla \left( \frac{P_{\parallel} - P_{\perp}}{B^2} \right) \\ &+ \left( \frac{1}{4\pi} - \frac{(P_{\parallel} - P_{\perp})}{B^2} \right) \mathbf{B} \times (\nabla \times \mathbf{B}) \\ &+ \frac{(P_{\parallel} - P_{\perp})}{B^2} \nabla \frac{B^2}{2}. \end{aligned}$$

We do not couple the dynamics to the double adiabatic CGL pressure equations. We are interested in scenarios in which  $P_{\parallel} - P_{\perp} > 0$  remains fixed as the firehose instability evolves, reflecting the presence of an energy source that prevents relaxation of the difference between the parallel and perpendicular pressures.

Let us use the subscript “0” to denote equilibrium quantities and let the magnetic field  $\mathbf{B}_0$  of a 2D geotail plasma equilibrium be represented as follows:

$$\mathbf{B}_0 = \nabla \psi(x, z) \wedge \nabla y, \quad (7)$$

where  $\psi$  is a flux function which labels the magnetic flux surfaces.

We introduce orthogonal curvilinear coordinates  $\psi, y, \chi$ , where  $(\psi, y)$  label a given field line and the third variable  $\chi$  is the field line coordinate. Note that  $\nabla \Phi_i \cdot \nabla \Phi_j = \delta_{ij}$ , where  $\Phi_1 = \psi$ ,  $\Phi_2 = y$ ,  $\Phi_3 = \chi$ , and  $\delta_{ij}$  is the Kronecker delta. The set of vectors  $\partial \mathbf{r} / \partial \psi$ ,  $\partial \mathbf{r} / \partial y$ ,  $\partial \mathbf{r} / \partial \chi$  is reciprocal to the set  $\nabla \psi$ ,  $\nabla y$ ,  $\nabla \chi$ , and we have  $\nabla \Phi_i \cdot \partial \mathbf{r} / \partial \Phi_j = \delta_{ij}$ . The equilibrium magnetic field can then be expressed as  $\mathbf{B}_0 = \nabla \psi \times \nabla y = \mathcal{J} \partial \mathbf{r} / \partial \chi$ , where  $\mathcal{J} = \nabla \psi \times \nabla y \cdot \nabla \chi = \mathbf{B}_0 \cdot \nabla \chi$ .

In plasma equilibria with  $P_{\perp} = P_{0\perp}(\psi, B_0)$ ,  $P_{\parallel} = P_{0\parallel}(\psi, B_0)$ , the parallel component of the force in Eq. (6) is

$$\begin{aligned} -\mathbf{b}_0 \cdot \nabla \frac{P_{0\parallel}}{B_0} - \frac{P_{0\perp}}{B_0^2} \mathbf{b}_0 \cdot \nabla B_0 \\ = -\frac{1}{B_0} \left( \frac{\partial P_{0\parallel}}{\partial B_0} + \frac{P_{0\perp} - P_{0\parallel}}{B_0} \right) \mathbf{b}_0 \cdot \nabla B_0 \end{aligned} \quad (8)$$

and it vanishes identically for a two-temperature Maxwellian phase space distribution function. The unit magnetic field vector is denoted by  $\mathbf{b}_0 = \mathbf{B}_0 / B_0$ .

The equilibrium pressure balance equation in the perpendicular direction is

$$\begin{aligned} \mathbf{b}_0 \times \nabla P_{0\perp} + \frac{1}{8\pi} \mathbf{b}_0 \times \nabla B_0^2 \\ = \left( \frac{B_0^2}{4\pi} + P_{0\perp} - P_{0\parallel} \right) \mathbf{b}_0 \times \boldsymbol{\kappa}_0, \end{aligned} \quad (9)$$

where  $\boldsymbol{\kappa}_0 = \mathbf{b}_0 \cdot \nabla \mathbf{b}_0$  is the field line curvature.

We assume zero perturbed parallel electric field typically small when the electron temperature is low and the electrons can respond to short out the parallel electric field perturbations.

Let the perturbed fields of the firehose mode be expressed in terms of the perturbed vector potential  $\delta \mathbf{A}$ :

$$\delta \mathbf{A} = \delta A_y(\chi, t) \nabla y, \quad (10)$$

where the mode is considered to be plane polarized (to simplify the analysis) and the mode propagates in the direction of the equilibrium field lines (so that  $\delta A_y$  is a function only of  $\chi$  and  $t$ ).

The perturbed electric and magnetic fields,  $\delta \mathbf{E}$  and  $\delta \mathbf{B}$ , are then given by

$$\delta \mathbf{E} = -\frac{1}{c} \frac{\partial \delta A_y}{\partial t} \nabla y, \quad (11)$$

$$\delta\mathbf{B} = \nabla \wedge \delta\mathbf{A} = \frac{\partial \delta A_y}{\partial \chi} \nabla \chi \wedge \nabla y = -\mathcal{J} \frac{\partial \delta A_y}{\partial \chi} \frac{\partial \mathbf{r}}{\partial \psi}. \quad (12)$$

Thus, for the total magnetic field  $\mathbf{B}$ , we have

$$\begin{aligned} \mathbf{B} &= \mathbf{B}_0 + \delta\mathbf{B} = \mathcal{J} \left( \frac{\partial \mathbf{r}}{\partial \chi} - \frac{\partial \delta A_y}{\partial \chi} \frac{\partial \mathbf{r}}{\partial \psi} \right) \\ &= \mathcal{J} \left\{ \left( \frac{\partial \mathbf{r}}{\partial \chi} \cdot \frac{\partial \mathbf{r}}{\partial \chi} \right) \nabla \chi \right. \\ &\quad \left. - \frac{\partial \delta A_y}{\partial \chi} \left( \frac{\partial \mathbf{r}}{\partial \psi} \cdot \frac{\partial \mathbf{r}}{\partial \psi} \right) \nabla \psi \right\}, \end{aligned} \quad (13)$$

where the second expression is an alternative representation of  $\mathbf{B}$  in terms of basis vectors  $\nabla\psi$ ,  $\nabla y$ , and  $\nabla\chi$ .

For  $\nabla \wedge \mathbf{B}$  we have

$$\begin{aligned} \nabla \times \mathbf{B} &= \left\{ \frac{\partial B_0^2}{\partial \psi \mathcal{J}} \right\} \nabla \psi \times \nabla \chi - \left\{ \frac{\partial \mathcal{J} \partial \delta A_y}{\partial \chi B_0^2 \partial \chi} \right\} \nabla \chi \\ &\quad \times \nabla \psi. \end{aligned} \quad (14)$$

Evaluating  $\mathbf{B} \times (\nabla \times \mathbf{B})$ , we obtain

$$\begin{aligned} \mathbf{B} \times (\nabla \times \mathbf{B}) &= \mathcal{J} \left\{ \left( \frac{\partial B_0^2}{\partial \psi \mathcal{J}} \right) \nabla \psi + \left( \frac{\partial \mathcal{J} \partial \delta A_y}{\partial \chi B_0^2 \partial \chi} \right) \nabla \psi \right\} \\ &\quad + \mathcal{J} \frac{\partial \delta A_y}{\partial \chi} \left\{ \left( \frac{\partial B_0^2}{\partial \psi \mathcal{J}} \right) \nabla \chi \right. \\ &\quad \left. + \left( \frac{\partial \mathcal{J} \partial \delta A_y}{\partial \chi B_0^2 \partial \chi} \right) \nabla \chi \right\}. \end{aligned} \quad (15)$$

The plasma velocity  $\mathbf{v}$  is approximated by the electric drift velocity,

$$\mathbf{v} = \frac{c}{B_0} \delta\mathbf{E} \times \mathbf{b}_0 + \dots = -\frac{1}{B_0^2} \frac{\partial \delta A_y}{\partial t} \nabla \psi, \quad (16)$$

where nonlinearities in the plasma inertia response and the mass density modulation  $\delta\rho$  associated with coupling to parallel acoustic waves are ignored.

Taking the  $\nabla\psi$  component of the CGL momentum equation, we obtain

$$-\rho \frac{\partial^2 \delta A_y}{\partial t^2} + \nabla \psi \cdot \left\{ \nabla \cdot \mathbf{P} + \frac{1}{4\pi} \mathbf{B} \times (\nabla \times \mathbf{B}) \right\} = 0, \quad (17)$$

where, keeping only the perturbed quantities and neglecting  $\partial/\partial\psi$  derivatives of the perturbed fields,

$$\begin{aligned} &\nabla \psi \cdot \left[ \nabla \cdot \mathbf{P} + \frac{1}{4\pi} \mathbf{B} \times (\nabla \times \mathbf{B}) \right] \\ &= \nabla \psi \cdot \mathbf{B} \mathbf{B} \cdot \nabla \frac{(P_{\parallel} - P_{\perp})}{B^2} \\ &\quad + \left( \frac{1}{4\pi} - \frac{(P_{\parallel} - P_{\perp})}{B^2} \right) \nabla \psi \cdot \mathbf{B} \times (\nabla \times \mathbf{B}) + \dots \end{aligned}$$

$$= \mathcal{J} B_0^2 \frac{\partial}{\partial \chi} \left( \frac{1}{4\pi} - \frac{(P_{\parallel} - P_{\perp})}{B^2} \right) \frac{\mathcal{J} \partial \delta A_y}{B_0^2 \partial \chi} + \dots \quad (18)$$

The perturbations vary predominantly along the field line and perpendicular gradients can be ignored.

Finally, we have the relevant nonlinear firehose equation

$$\rho \frac{\partial^2 \delta A_y}{\partial t^2} = \frac{\mathcal{J}}{4\pi} B_0^2 \frac{\partial}{\partial \chi} \left( 1 - \frac{4\pi(P_{\parallel} - P_{\perp})}{B^2} \right) \frac{\mathcal{J} \partial \delta A_y}{B_0^2 \partial \chi}, \quad (19)$$

where the total field magnitude (equilibrium plus perturbed) is given by

$$B^2 = B_0^2 + \frac{\mathcal{J}^2}{B_0^2} \left( \frac{\partial \delta A_y}{\partial \chi} \right)^2. \quad (20)$$

Having completed the vector calculus calculation using the orthogonal coordinates  $(\psi, y, \chi)$ , we revert to the usual distance measured along the field line  $s=s(\chi, \psi)$  coordinate, to replace the field line coordinate  $\chi$ . Then, in a given flux tube with  $\psi$  constant, we have  $(\mathcal{J}/B_0) \partial \delta A_y / \partial \chi = \partial \delta A_y(s, \psi) / \partial s$  and the magnetic field magnitude is given by  $B^2 = B_0^2(s, \psi) + [\partial \delta A_y(s, \psi) / \partial s]^2$ .

In Sec. II, we discussed the dispersion relation for parallel propagating circularly polarized modes in a uniform homogeneous plasma. The mode amplitude is  $\delta A_{\pm} = \delta A_x \pm i \delta A_y$  (with  $\delta A_x = 0$ ,  $\delta A_y \neq 0$  for a right-hand circularly polarized mode) and the square of the perturbed magnetic field magnitude is  $|\partial \delta A_{\pm} / \partial z|^2$ . In a dipole field configuration, it is typically the case that the parallel wavelengths of the perturbations are less than the scale length of the variation of the equilibrium magnetic field along the field line [see Sec. V] and in this limit, the generalization of Eq. (19) to a circularly polarized mode is achieved as follows: the mode amplitude  $\delta A_y$  is replaced by  $\delta A = \delta A_{\perp}$  and the square of the magnetic field magnitude  $B^2$  by  $B^2 = B_0^2 + |\partial \delta A / \partial s|^2$ .

Note the presence in Eq. (19) of the firehose stability parameter  $\sigma$  defined by

$$\sigma = \left( 1 - \frac{A}{1 + \frac{\mathcal{J}^2}{B_0^4} \left| \frac{\partial \delta A}{\partial s} \right|^2} \right),$$

where the firehose anisotropy parameter  $A$  is given by

$$A = \frac{4\pi(P_{\parallel} - P_{\perp})}{B_0^2}.$$

We have assumed that  $P_{\parallel} - P_{\perp} > 0$  remains constant, and the nonlinearity in Eq. (19) manifests itself through the square of the total magnetic field  $B^2$ .

The firehose anisotropy parameter is assumed to be greater than unity,  $A > 1$ . Thus, in a uniform homogeneous plasma,  $\sigma < 0$  for negligibly small magnetic field perturbations and the firehose mode is unstable. However, as the magnetic field perturbations grow in amplitude, the value of  $\sigma$  approaches and eventually exceeds zero and linear wave growth is significantly modified.

In a dipole equilibrium,  $\sigma$  is typically positive except at the ‘‘equatorial plane’’ where the magnetic field attains its minimum value. With boundary condition  $\delta A(s=\pm L)=0$  at

the ends of the field line, the linear eigenmodes are discrete, and the number of unstable modes will depend on the extent of the field line over which the firehose stability parameter is negative  $\sigma < 0$ . The most unstable mode is the odd parity mode, with  $\delta A(s)$  antisymmetric in  $s$  and the magnetic field perturbation a maximum at the equatorial plane. In Sec. V, we describe the numerical simulation of Eq. (19), and as will be seen the nonlinear evolution of the firehose instability in a dipole field will depend on the proximity of the equilibrium to the marginally stable state.

Let us now discuss the modifications to Eq. (19) introduced by resistive and viscous dissipations as well as kinetic dispersion.

#### IV. FIREHOSE PDE MODIFIED BY DISSIPATION AND DISPERSION

In this section, we modify the nonlinear firehose equation [Eq. (30)] by including the effects of (1) plasma resistivity and viscosity which dissipates the energy in short wavelength turbulence generated by the firehose instability and (2) mode dispersive effects due to ion kinetics as described in Sec. II.

From Ohm's law, Eq. (16) for the perturbed plasma velocity is modified in a resistive plasma as follows:

$$\begin{aligned} \mathbf{v} &= \frac{c}{B_0} (\delta \mathbf{E} - \bar{\eta} \delta \mathbf{J}) \times \mathbf{b}_0 \\ &= -\frac{1}{B_0} \left( \frac{\partial \delta A_y}{\partial t} - \frac{\bar{\eta} c^2 B_0}{4\pi} \frac{\partial}{\partial s} \frac{1}{B_0} \frac{\partial \delta A_y}{\partial s} \right) \frac{\nabla \psi}{B_0}, \end{aligned} \quad (21)$$

where  $\bar{\eta}$  is the plasma resistivity.

Similarly, plasma viscosity  $\bar{\mu}$  is included by introducing an additional term to the force balance equation [Eq. (6)], with  $\rho \partial \mathbf{v} / \partial t$  changed to

$$\rho \frac{\partial \mathbf{v}}{\partial t} - \frac{\bar{\mu}}{B_0} \frac{\partial}{\partial s} \frac{1}{B_0} \frac{\partial}{\partial s} B_0^2 \mathbf{v}. \quad (22)$$

We find it convenient to parametrize the resistivity  $\bar{\eta}$  and viscosity  $\bar{\mu}$  as follows:

$$\frac{c \bar{\eta}}{4\pi} = \frac{B_0^2}{4\pi \rho} \eta = V_A^2 \eta,$$

$$\bar{\mu} = \frac{B_0^2}{4\pi} \mu = \rho V_A^2 \mu,$$

where  $\eta$  and  $\mu$  are parameters which have the dimension of time.

Then, substituting Eq. (21) for  $\mathbf{v}$  we have

$$\begin{aligned} \rho \frac{\partial \mathbf{v}}{\partial t} - \frac{\bar{\mu}}{B_0} \frac{\partial}{\partial s} \frac{1}{B_0} \frac{\partial}{\partial s} B_0^2 \mathbf{v} &= \left\{ -\frac{\rho}{B_0^2} \frac{\partial^2 \delta A_y}{\partial t^2} + \frac{B_0}{4\pi} \frac{\partial}{\partial s} \left[ \frac{\eta + \mu}{B_0} \frac{\partial^2 \delta A_y}{\partial t \partial s} \right. \right. \\ &\quad \left. \left. - \frac{1}{B_0} \frac{\partial}{\partial s} \eta \mu V_A^2 B_0 \frac{\partial}{\partial s} \frac{1}{B_0} \frac{\partial \delta A_y}{\partial s} \right] \right\} \nabla \psi. \end{aligned}$$

Thus, including plasma resistivity and viscosity as described above, and also dispersive effects described by Eq. (5), we modify Eq. (19) to obtain the final form of the nonlinear PDE for the firehose mode:

$$\begin{aligned} \frac{\rho}{B_0^2} \frac{\partial^2 \delta A}{\partial t^2} &= \frac{B_0}{4\pi} \frac{\partial}{\partial s} \left[ \frac{\sigma}{B_0} \frac{\partial \delta A}{\partial s} + \frac{\mu_3 + i\nu}{B_0} \frac{\partial^2 \delta A}{\partial t \partial s} \right. \\ &\quad \left. - \frac{1}{B_0} \frac{\partial}{\partial s} \mu_4 V_A^2 B_0 \frac{\partial}{\partial s} \frac{1}{B_0} \frac{\partial \delta A}{\partial s} \right] \end{aligned} \quad (23)$$

where  $\mu_3 = \eta + \mu$ ,  $\mu_4 = \eta \mu$  and  $\nu = \{(1 + (\beta_{ii}/2)) / \Omega_i\}_{s=0}$  is the coefficient of the dispersive term described in Sec. II. As will be seen in Sec. IV, the form of Eq. (23) allows us to derive an energy equation which is used to monitor the accuracy of the numerical simulations.

We impose the boundary condition  $\delta A(s = \pm L) = 0$  at the ends of the field line  $s = \pm L$ , implying that we are modeling the ionosphere or low altitude (high  $B$  field) region as a boundary with perfect energy reflection.

The viscosity and resistivity used to absorb the energy on the subgrid scale turbulence may be thought of as a proxy for the effect of the high frequency  $\omega \sim \omega_{pi}$  lower hybrid drift (LHDI) wave turbulence seen in the flow bursts.<sup>7</sup> When no viscous-resistive dissipation is included the cross-field current density in the large scale Alfvénic fluctuations exceeds the threshold for the current driven lower hybrid modes of Huba *et al.*<sup>10,11</sup> This LHDI turbulence is clearly a candidate to produce the dissipation used in modeling the subgrid scale dissipation given by the viscosity and resistivity in the simulation model developed here. To include the coupling of the LHDI to the firehose Alfvén turbulence will require new multiscale simulation codes.

#### V. ENERGY CONSERVATION

In this section, we derive the equation for energy conservation.

Multiplying Eq. (23) by  $\partial \delta A^* / \partial t$  and integrating the resulting equation over a field line, we obtain

$$\begin{aligned} \int_{-L}^L \frac{ds}{B_0} \frac{\partial \delta A^*}{\partial t} \left\{ \frac{\rho}{B_0^2} \frac{\partial^2 \delta A}{\partial t^2} - \frac{B_0}{4\pi} \frac{\partial}{\partial s} \left[ \frac{\sigma}{B_0} \frac{\partial \delta A}{\partial s} \right. \right. \\ \left. \left. + \frac{\mu_3 + i\nu}{B_0} \frac{\partial^2 \delta A}{\partial t \partial s} - \frac{1}{B_0} \frac{\partial}{\partial s} \mu_4 V_A^2 B_0 \frac{\partial}{\partial s} \frac{1}{B_0} \frac{\partial \delta A}{\partial s} \right] \right\} = 0. \end{aligned}$$

The complex conjugate of the above equation is

$$\begin{aligned} \int_{-L}^L \frac{ds}{B_0} \frac{\partial \delta A}{\partial t} \left\{ \frac{\rho}{B_0^2} \frac{\partial^2 \delta A^*}{\partial t^2} - \frac{B_0}{4\pi} \frac{\partial}{\partial s} \left[ \frac{\sigma}{B_0} \frac{\partial \delta A^*}{\partial s} \right. \right. \\ \left. \left. + \frac{\mu_3 - i\nu}{B_0} \frac{\partial^2 \delta A^*}{\partial t \partial s} - \frac{1}{B_0} \frac{\partial}{\partial s} \mu_4 V_A^2 B_0 \frac{\partial}{\partial s} \frac{1}{B_0} \frac{\partial \delta A^*}{\partial s} \right] \right\} = 0. \end{aligned}$$

Summing these equations and integrating by parts with the boundary condition  $\delta A(s = \pm L) = 0$ , we obtain the following equation for energy conservation:

$$\frac{d}{dt} (W_K + W_B - W_P + W_V) = -P_V, \quad (24)$$

where the magnetic energy  $W_B$  and kinetic energy  $W_K$  are defined as follows:

$$W_K = \frac{1}{2} \int \frac{ds}{B_0} \frac{\rho}{B_0^2} \left| \frac{\partial \delta A}{\partial t} \right|^2 \Big/ \int \frac{ds}{B_0}, \quad (25)$$

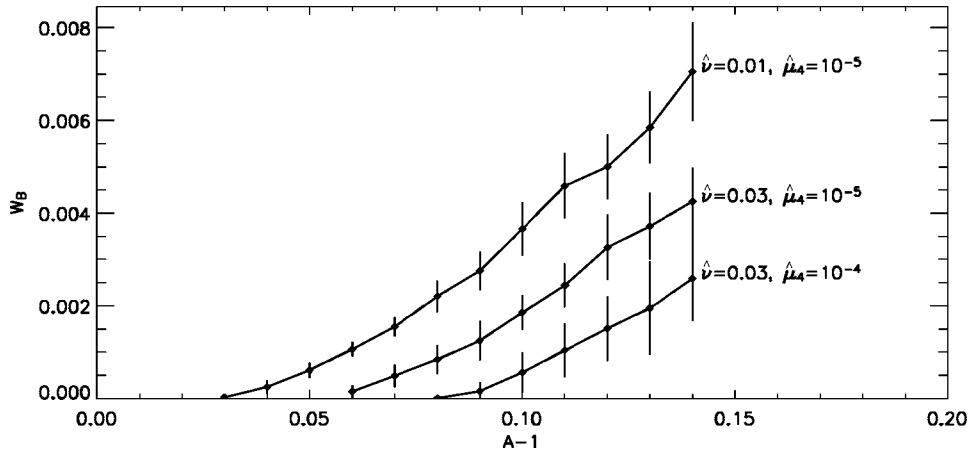


FIG. 1. Plots of saturated  $W_B$  as functions of equatorial  $A_0-1$  for different  $\hat{\nu}$  and  $\hat{\mu}_4$ . In all simulations, the plasma pressure  $p_{\perp}$ , magnetic field  $B_0$ , and number of grid points are the same in cases 1, 2, and 3, as given in Table I.

$$W_B = \frac{1}{8\pi} \int \frac{ds}{B_0} \left| \frac{\partial \delta A}{\partial s} \right|^2 \bigg/ \int \frac{ds}{B_0}, \quad (26)$$

and the quantities  $W_P$ ,  $W_V$ , and  $P_V$ , are defined by

$$W_P = \frac{1}{8\pi} \int \frac{ds}{B_0} A B_0^2 \ln \left( 1 + \frac{1}{B_0^2} \left| \frac{\partial \delta A}{\partial s} \right|^2 \right) \bigg/ \int \frac{ds}{B_0}, \quad (27)$$

$$W_V = \frac{1}{8\pi} \int \frac{ds}{B_0} \mu_4 V_A^2 \left| B_0 \frac{\partial}{\partial s} \frac{1}{B_0} \frac{\partial \delta A}{\partial s} \right|^2 \bigg/ \int \frac{ds}{B_0}, \quad (28)$$

$$P_V = \frac{1}{4\pi} \int \frac{ds}{B_0} \mu_3 \left| \frac{\partial^2 \delta A}{\partial t \partial s} \right|^2 \bigg/ \int \frac{ds}{B_0}. \quad (29)$$

Note that  $W_B$ ,  $W_K$ ,  $W_V$ , and  $P_V$  are positive definite, and  $W_P$  is positive for anisotropic plasma pressures with  $p_{\parallel} > p_{\perp}$ .  $W_P$  represents the energy source driving the firehose instability, while  $P_V$  is the energy damping rate due to resistivity and viscosity.

The boundary condition  $\delta A(s = \pm L) = 0$  implies that we are modeling the ionosphere or low altitude (high  $B$  field) region as a boundary with perfect energy reflection.

We monitor Eq. (24) as an estimate of the accuracy of the linear and nonlinear simulations. Figure 1 shows plots of the energy  $W_B \approx \langle \delta B_{\perp}^2 / 2 \rangle_L / B^2 \approx (\Delta s / L) \langle \delta B_{\perp}^2 / 2 \rangle_{\Delta s} / B^2$  as a function of  $A$  and  $\nu$  for the simulations described in Sec. VII, where  $\langle \rangle_L$  is a flux tube average of length  $l$  and  $\Delta s$  is the full width scale length at half-maximum of  $\delta B_{\perp}(s)$ . Thus we can estimate the turbulence magnitude at the central part of the field line as  $\delta B_{\text{rms}} / B_n = (L / \Delta s)^{1/2} \sqrt{2W_B}$ .

## VI. NUMERICAL SIMULATIONS

The nonlinear partial differential equation for the firehose mode is solved as an initial value problem by using the Runge–Kutta fourth-order method. The equilibrium magnetic field is taken to be that of the simple finite dipolelike  $\beta$  equilibrium field model given by Chan *et al.*,<sup>12</sup> recognizing, however, that this field model is not consistent with a high- $\beta$  plasma. We do not expect our results to be sensitive to the specific details of the field line variation of the dipole magnetic field magnitude. The mirror ratio is controlled by the maximum value of the length  $L$  of the magnetic field line. All  $s$  derivatives are determined by a cubic spline interpolation on a grid with spacing  $\Delta s = L/N$  and  $N = 129$ .

The key dimensionless physical parameters are the anisotropy factor  $A_0 = 4\pi(p_{\parallel} - p_{\perp}) / B_n^2$ , the plasma beta  $\beta_{\parallel} = 8\pi p_{\parallel} / B_n^2$ , and the dispersion parameter  $\hat{\nu} = V_{0A} / L\nu$ , where  $B_n = B_0(s=0)$  and  $V_{0A} = V_A(s=0)$ .

We choose plasma parameters characteristic of flux tubes located at a radius of  $R = 12R_E$ . At the quatorial plane, we take the Alfvén speed to be  $V_A = 500$  km/s,  $T_{\parallel i} / T_{\perp i} = 1.44$ , and  $\beta_{\parallel i} = 7.2$ , so that the anisotropy parameter is  $A_0 = 1.1$ .

As mentioned earlier, we find it necessary to keep finite hyperviscosity ( $\hat{\mu}_4 \equiv (V_{0A} / L)\mu_4 > 0$ ) in order to control the nonlinear buildup of fluctuation energy on the grid scale during the extended nonlinear phase of the time evolution. Simulations with  $\hat{\mu}_4 = 0$  have the problem that energy conservation, as determined by Eq. (24), is not satisfied in the extended nonlinear phase of the simulation due to the accumulation of fluctuation energy on the grid scale.

In Table I, we list the magnitude of the parameters  $\hat{\nu}$  and  $\hat{\mu}_4$  for three different simulations. In Fig. 1 we summarize the magnetic energy in Alfvén-type fluctuations for the three

TABLE I. Parameters for three simulation cases.

Case	Type	$A_0-1$	$\beta_{\perp}$	$\hat{\nu}$	$R_m$	$N\Delta x$	$\hat{\mu}_4$	$W_B$
1	Solitonlike	0.1	5.0	0.03	3	129	$10^{-4}$	$(0.58 \pm 0.43) \times 10^{-3}$
2	Weak turbulence	0.1	5.0	0.03	12	129	$10^{-5}$	$(1.82 \pm 0.45) \times 10^{-3}$
3	Strong turbulence	0.1	5.0	0.01	12	129	$10^{-5}$	$(3.74 \pm 0.52) \times 10^{-3}$

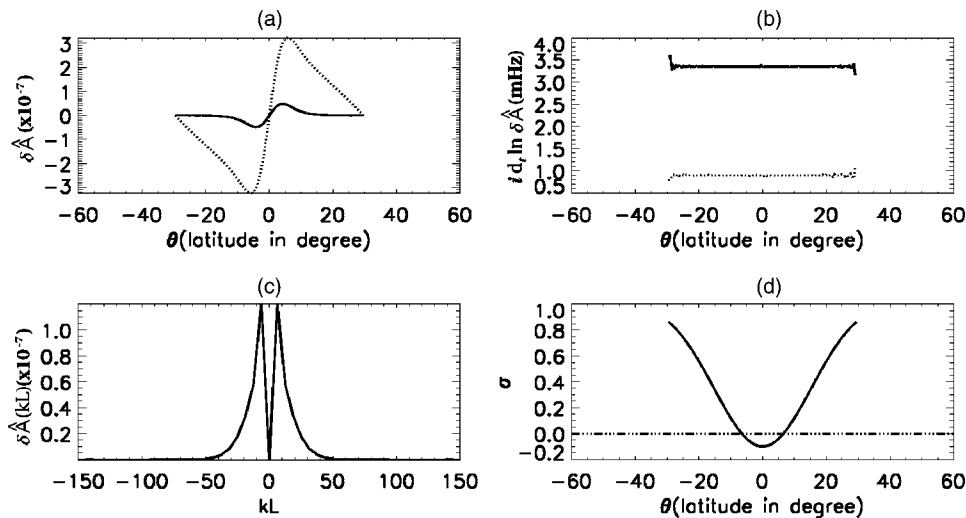


FIG. 2. Most unstable eigenmode in the linear stage of the simulation for the soliton bursts, case 1. As in Figs. 5 and 8, (a) is the most unstable eigenmode  $\delta\hat{A}=\delta A/(B_n L)$ , (b) the local angular frequency (solid line) and growth rate (dotted line) of the most unstable mode, (c) the absolute value of the parallel wave number spectrum of the eigenmode, and (d) the linear firehose parameter  $\sigma$  as a function of  $\theta$ .

cases as a function of the anisotropy drive parameter ( $A_0 - 1$ ). Increasing the dispersion parameter  $\hat{\nu}$  reduces the turbulence levels by one-half, as shown in Table I. In Figs. 2–10 we present the detailed results of the numerical simulations.

### A. Case 1: Soliton behavior

In case 1, with  $\hat{\nu}=0.03$  and  $\hat{\mu}_4=10^{-4}$ , the equilibrium state is close to marginal stability.

Figure 2 displays the most unstable eigenmode as a function of latitude  $\theta=(\pi s/2L)$  in panel (a), its real frequency (solid line) and growth rate (dotted line) in panel (b), and its wave number spectrum in panel (c).

The magnitude of the firehose stability parameter  $\sigma$  as a function of  $\theta$  is plotted in panel (d). The firehose parameter  $\sigma$  is negative only within a small central range of the field line,  $\Delta L/L \approx 0.1$ . Free energy from this range of  $\sigma < 0$  excites the firehose instability locally, which then propagates along the whole field line, and thus finally leads to a global firehose mode.

The smallest wavelength component of the eigenmode is typically of the order of the spatial width  $\Delta L \approx 0.1 L$  of the region within which  $\sigma$  is negative. This can be seen from panel (c) where we estimate the wave number maximum  $k_{\max}$

to be  $k_{\max}L \approx 20\pi$ , i.e.,  $k_{\max}\Delta L = k_{\max}L\Delta L/L \sim 2\pi$ . A similar result will also be seen later in Figs. 5 and 8.

Figure 3(a) shows the time dependence of  $\delta B(s=0, t) = |\partial\delta A/\partial s|_{s=0}$  after saturation of linear wave growth. The saturation amplitude is  $\approx \delta B/B_n \sim 0.07$ . In the nonlinear stage, there are periodic bursts of low-amplitude fluctuations at approximately every 35 min. Each burst lasts about 20 min, with four cycles of  $\delta B$  in each burst. The frequency spectrum is a band of frequencies of width  $\Delta f/f \sim 0.5$ , centered at  $f \sim 3.5$ –4 mHz, as shown in Fig. 3(b).

The time evolution of the instability exhibits a soliton-like behavior. Note that the wave number spectrum of the unstable eigenmode [see Fig. 2(c)] is narrow. A coherent unstable mode grows and saturates at a low amplitude. Thereafter, the mode decays and returns to its initial state where it lingers until the linear eigenmode can again form and grow, and the cycle of growth and decay is repeated.

In Fig. 4, we plot the time dependence of the flux tube averaged energies  $W_B$ ,  $W_P$ ,  $W_K$ , and  $W_{\text{total}}$ . Energy from the anisotropy source  $W_P$ , driving the firehose instability, is converted predominantly into magnetic energy  $W_B$  and vice versa.

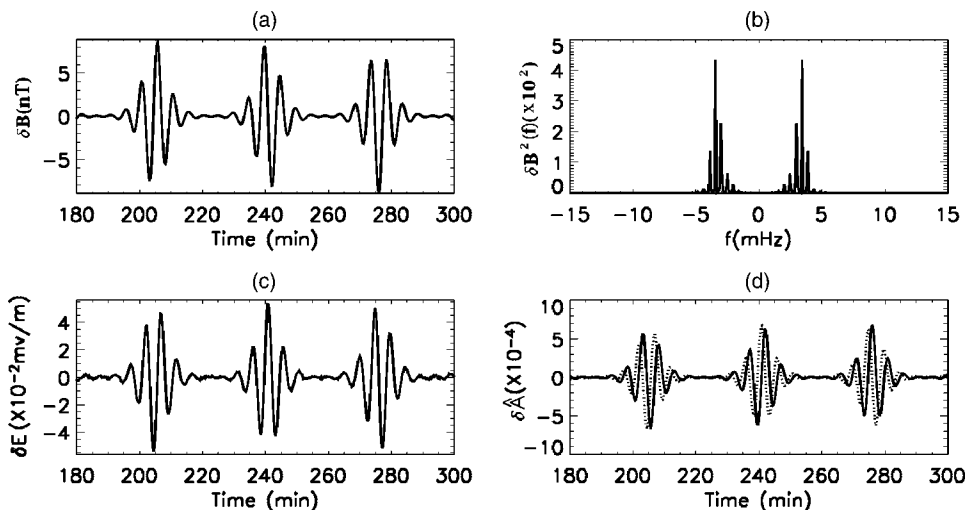


FIG. 3. Two hours saturated nonlinear fluctuations at  $\theta=0$  in nonlinear stage of simulation for the soliton bursts. There are periodic bursts of soliton behavior in (a)  $\delta B=(\partial/\partial s)\delta\hat{A}$ , (c)  $\delta E=(-1/c)(\partial/\partial t)\delta\hat{A}$ , and (d)  $\delta\hat{A}$ . Panel (b) is the turbulent magnetic energy frequency spectrum.

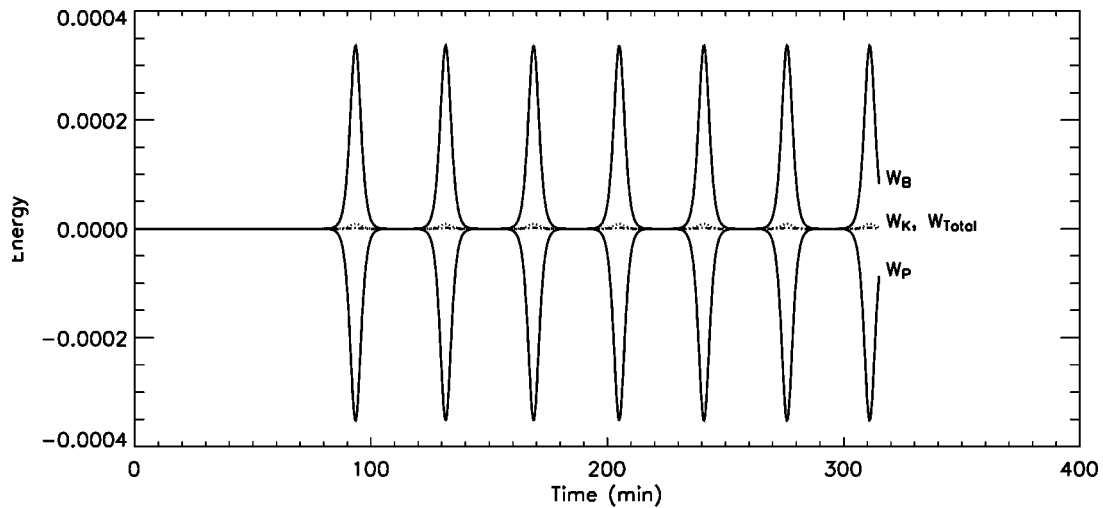


FIG. 4. Time dependence of flux tube averaged energies  $W_B$ ,  $W_K$ ,  $W_P$ , and  $W_{\text{total}}$  in the nonlinear firehose simulation for the soliton bursts. Exponentially growing  $W_B$  (which cannot be seen in this linear-linear plot) is in the linear stage for  $t < 80$  min. There are seven pulses from the solitons separated by 35 min with a full width at half maximum of  $\sim 3$  min.

### B. Case 2: Weak turbulence

In case 2, the magnitude of the dispersive parameter  $\hat{\nu} = 0.03$  is the same as that in case 1, but the dissipation parameter  $\hat{\mu}_4 = 10^{-5}$  is smaller by an order of magnitude. The equilibrium is further away from marginal stability, and the dissipation and damping of short wave length modes are reduced.

Figure 5 displays the most unstable eigenmode in panel (a), its frequency in panel (b), its wave number spectrum in panel (c), and the value of  $\sigma$  in panel (d). The unstable mode structure is similar to that of Case 1 but the linear growth rate is larger.

Figure 6(a) shows the time dependence of  $\delta B(s=0, t) = |\partial \delta A / \partial s|_{s=0}$  after saturation of linear wave growth and Fig. 6(b) the frequency spectrum. The saturation amplitude is  $\approx \delta B/B_n \sim 0.12$ , larger than that in case 1. The nonlinear coupling to other modes is no longer ignorable and the nonlinear state is not dominated by a single coherent mode. The amplitude fluctuations remain finite with  $\delta B(s=0)$  varying approximately sinusoidally.

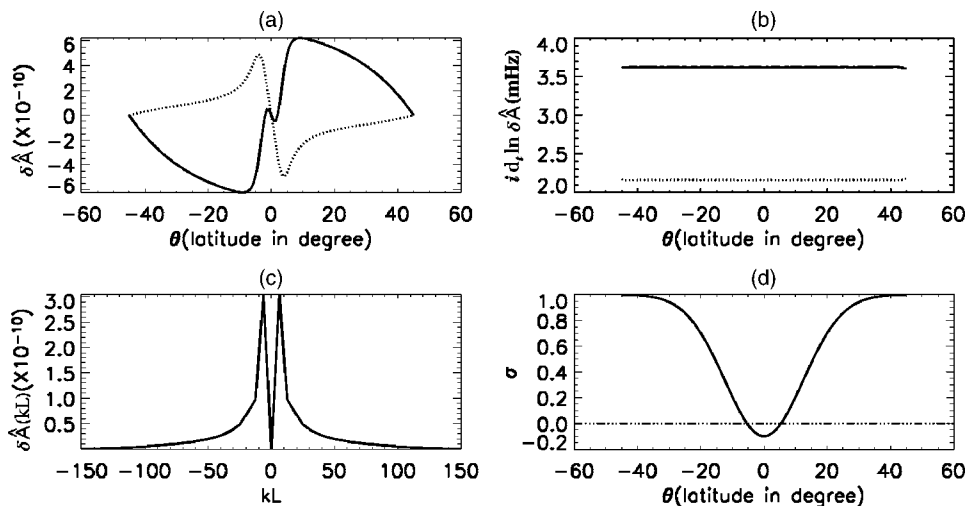


FIG. 5. Most unstable eigenmode in the linear stage of the simulation, case 2. As in Fig. 2 (a) gives the most unstable eigenmode as a function of  $\theta$ , (b) gives  $i \partial \ln \delta A / \partial t$  along a field line, (c) gives the absolute value of the parallel wave number spectrum of the eigenmode, and (d) gives the linear firehose parameter  $\sigma$  as a function of  $\theta$ .

In Fig. 7, we plot the time dependence of the flux tube averaged energies  $W_B$ ,  $W_P$ ,  $W_K$ , and  $W_{\text{total}}$ . Energy from the anisotropy source  $W_P$ , driving the firehose instability, is converted predominantly into magnetic energy  $W_B$ . The flux tube averaged fluctuation amplitude is estimated to be  $\delta B/B_0(0) \sim 0.06$ .

### C. Case 3: Strong turbulence

In case 3, the dispersive parameter is reduced to  $\hat{\nu} = 0.1$  and the dissipation parameter is the same as that in case 2  $\hat{\mu}_4 = 10^{-5}$ .

Figure 8 displays the unstable eigenmode in panel (a) as a function of latitude  $\theta = \pi s / (2L)$ , its real frequency (solid line) and growth rate (dotted line) in panel (b), its wave number spectrum in panel (c), and the value of  $\sigma$  in panel (d).

The linear growth rate for this case is larger than that in case 2, and the equilibrium state is even further away from marginal stability.

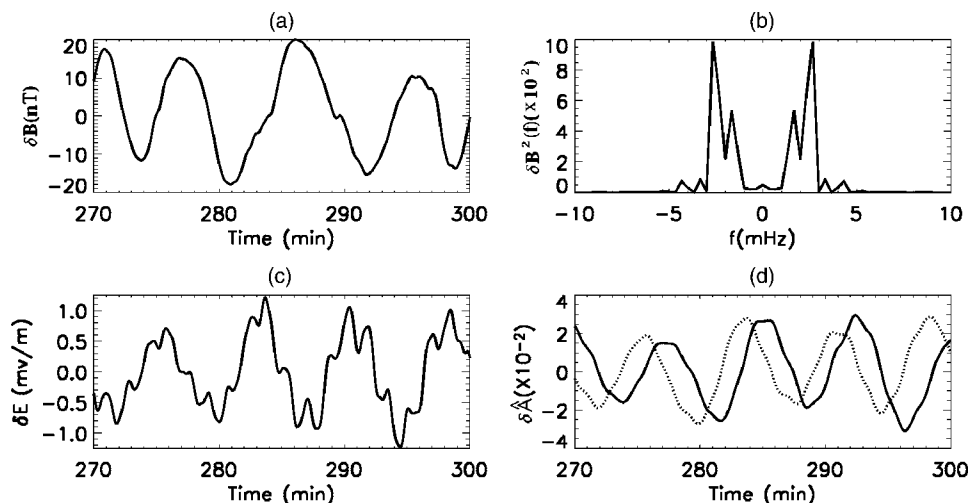


FIG. 6. Thirty minutes of saturated nonlinear fluctuations at  $\theta=0$  in the nonlinear stage of simulation, case 2. As in Fig. 2 (a) gives the turbulent  $\delta B$ , (b) gives the turbulent magnetic energy spectrum, (c) gives the turbulent  $\delta E$ , and (d) gives the turbulent  $\delta A$ .

Figure 9 shows the turbulence for 20 min of constant anisotropy driving,  $A=1.1$ , at the equator. We see strong turbulence of the perturbed magnetic field  $\delta B(s=0, t)$  with high amplitudes in panel (a). The saturation amplitude is  $\approx \delta B/B_n \approx 13/50$ , where  $B_n=50$  nT is the magnitude of the equilibrium field at the equatorial plane. Panel (b) displays the frequency spectrum.

The real frequencies in the nonlinear-state [see Fig. 9(b)] are much lower than the real frequency of the linearly unstable mode [see Fig. 8(b)]. Thus there is a significant downward shift in the real frequency as the instability evolves into the nonlinear phase.

In panel (c) we see a spiky electric field and in panel (d) the Faraday rotation of the displacement vector.

Figure 10 shows energy conservation during the nonlinear firehose simulation. The magnetic energy  $W_B$  grows exponentially in the linear stage,  $t < 16$  min. Beyond  $t \geq 20$  min there are many interacting modes producing the irregular fluctuations in the saturated nonlinear stage. Figure 10 also gives the flux tube averaged turbulence amplitude as

$\overline{\delta B}/B_n \approx \sqrt{2W_B} \sim 0.086$ . The average amplitude in the small range  $\Delta s$ , within which the firehose instability is driven, is larger than the global amplitude  $\overline{\delta B}/B_0$  by  $\approx \delta B_{\text{rms}}/B_n = (L/\Delta s)^{1/2} \overline{\delta B}/B_n$ .

## VII. COMPARISON OF DRIVEN FIREHOSE TURBULENCE WITH PI-2 FLUCTUATIONS

Magnetic field fluctuations in the Pi-2 frequency range 7–30 mHz are routinely observed at and before the start of magnetic field dipolarization in substorms. There are apparently three varieties of Pi-2 fluctuations according to Kepko and Kivelson,<sup>5,6</sup> with one type of Pi-2 turbulence well correlated with the high-speed earthward-flow burst  $v_x = E_y/B_x \approx 800\text{--}1000$  km/s. Such fast earthward plasma flows are expected to drive up the parallel pressure of the ions faster than the perpendicular pressure, producing the firehose instability.<sup>2,3</sup> Thus, we seek to correlate these particular Pi-2 fluctuations with the nonlinear firehose electromagnetic turbulence derived here.

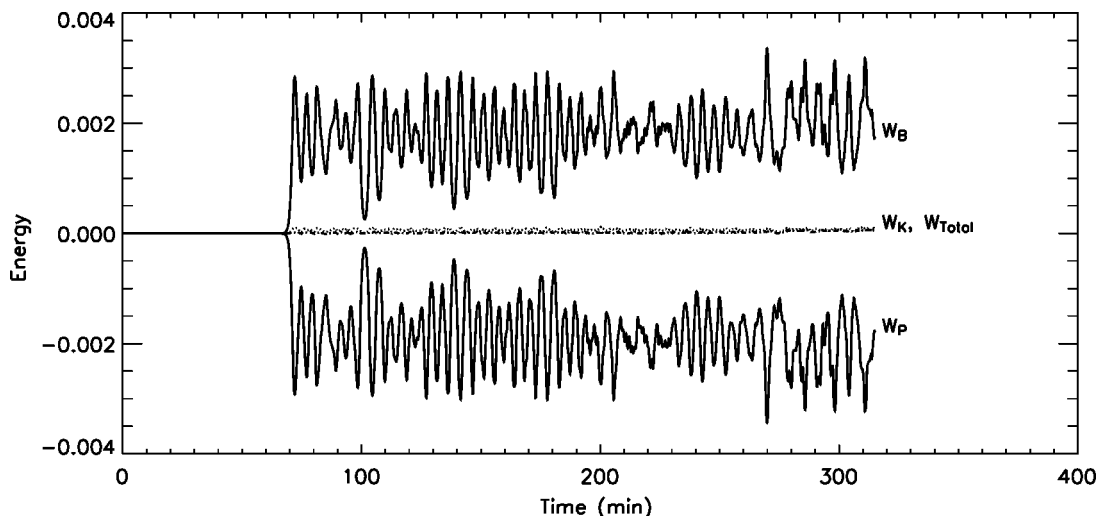


FIG. 7. Time dependence of flux tube averaged energies  $W_B$ ,  $W_K$ ,  $W_P$ , and  $W_{\text{total}}$  in the nonlinear firehose simulation, case 2. The magnetic energy  $W_B$  grows exponentially in linear stage up to 70 min and then becomes saturated turbulence in the nonlinear stage. As same in Fig. 4,  $W_B \approx -W_P$  is much larger than  $W_K$ ,  $W_{\text{total}}$  remains very small, and  $W_V$  is very small and therefore not plotted.

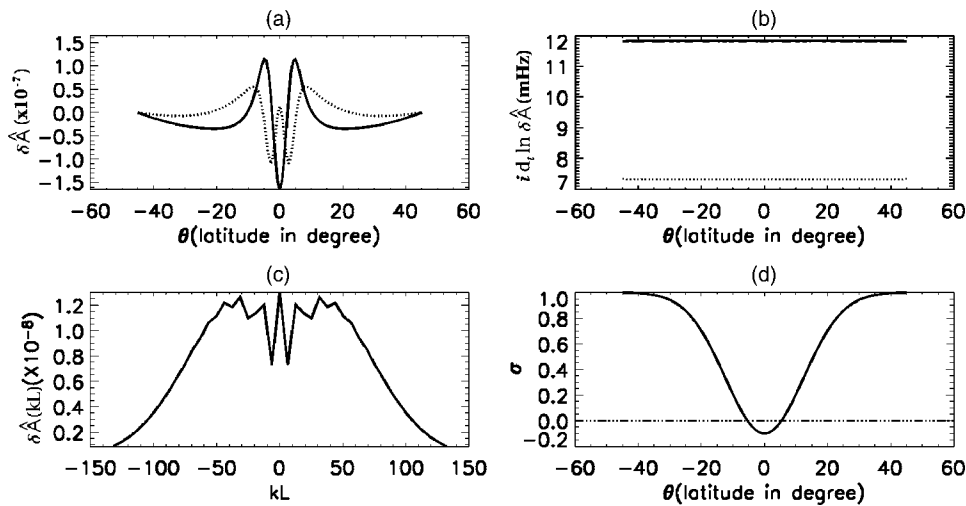


FIG. 8. Unstable eigenmode in the linear stage of the simulation for the strong turbulence, case 3: (a) most unstable eigenmode as a function of latitude  $\theta$ , where solid line is the real part and dotted line is the imaginary part; (b) real part (solid line) and imaginary part (dotted line) of  $i \partial \ln \delta A / \partial t$  along a field line; (c) absolute value of the parallel wave number spectrum of the eigenfunction  $\delta A(k_{\perp} L)$  in mode number space; and (d) linear firehose parameter  $\sigma$  as a function of  $\theta$ .

Sigsbee *et al.* show the characteristics of this type of substorm-flow burst Pi-2 turbulence for five substorms from the geotail spacecraft in the region of  $10R_E$ – $13R_E$ . The geotail electric and magnetic data shown in Fig. 3 of Ref. 7 for the April 26, 1995 substorm at 0750UT show broadband Pi-2 fluctuations in the frequency range  $f \approx 3$ –30 mHz for durations  $\Delta t \leq 10$  min. During this time interval, called the dipolarization front, the mean  $B_x$  field decreases from 40 nT to 10 nT and  $B_z$  increases from 5 nT to 20 nT for the April 26, 1995 substorm with geotail 3 s magnetometer data at  $13R_E$  near 23:00 MLT (MLT—mass-length-time). The earthward flow reaches 2000 km/s such that  $E_y = v_x B_z \sim 50$  mV/m at 0754UT where the  $\delta B$  fluctuations reach their maximum level. All three components of  $B$  are spiky, with a turbulent wave form showing perhaps up to 100 spikes in the 15 min period containing some smaller amplitude noise up to 100 mHz. The ion cyclotron frequency starts at 600 mHz and drops to 300 mHz (Ref. 7, Fig. 4).

The low-frequency spectrum is such that  $\omega / \Omega_i \sim 0.03$ – $0.10$  and  $\delta B / B \approx 10 \text{ nT} / 40 \text{ nT} = 0.25$ . Furthermore, the noisy wave forms reported in (Ref. 7, Fig. 3) for  $B_x$ ,  $B_y$ ,  $B_z$ , and  $E_y$  are similar to those obtained for a 10 min interval in the simulations shown in our Fig. 9. Thus, we conclude that the nonlinear firehose turbulence is capable of explain-

ing both the correlation of the turbulence with the fast earthward flows and the observed characteristics of the electromagnetic turbulence for these types of Pi-2 oscillations.

There appear to be no observations which directly correlate Pi-2 fluctuations with negative values of the firehose stability parameter  $\sigma_0$ :  $\sigma = 1 - A_0 < 0$ , where  $A_0$  is the anisotropy parameter defined by  $A_0 = 4\pi(P_{\parallel} - P_{\perp}) / B^2$ . However, there is evidence of the occurrence of negative values of  $\sigma_0$  in the Earth's geotail. Kaufmann *et al.* used one year of one-minute geotail data to analyze the firehose anisotropy parameter  $A_0$  as a function of the plasma  $\beta = 8\pi P_{\parallel} / B^2$ . They reported values for  $A_0$  ranging from  $-0.1$  to  $+1.25$ , with the values near to zero occurring in the high- $\beta$  bins.<sup>13</sup> The number of data samples in the high- $\beta$  bins,  $\beta > 30$  and  $10 < \beta < 30$ , is, however, low. For example, in the region near  $X = -10R_e$  for  $|Y| \leq 15R_e$ , Kaufmann *et al.* found 1425 cases with  $0 < A_0 < 0.25$  and 32 cases with  $1 \leq A_0 < 1.25$ . They concluded that even though the values of  $A_0$  from the data is a few tenths, the methodology that was used underestimates the value of  $A_0$ .

In the firehose simulations, the time scales and magnitudes of the computed fluctuations are consistent with the magnetic and electric fluctuation observations reported by

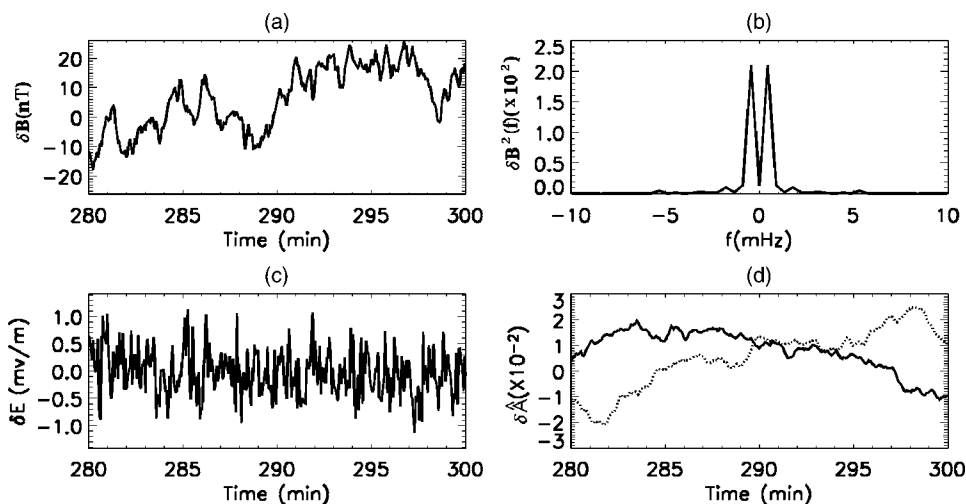


FIG. 9. Twenty minutes of saturated nonlinear fluctuations at  $\theta = 0$  in the nonlinear stage of the simulation. Here (a) is the turbulent perpendicular magnetic field  $\delta B$ , (b) is the turbulent magnetic energy frequency spectrum, (c) is the turbulent down-dusk electric field  $\delta E$ , and (d) gives the real (solid line) and imaginary (dotted line) parts of the turbulent vectorial potential  $\delta A$ . The magnitudes in (a) and (b) are estimated based on choosing the field  $B_0 = 50$  nT at  $\theta = 0$ .

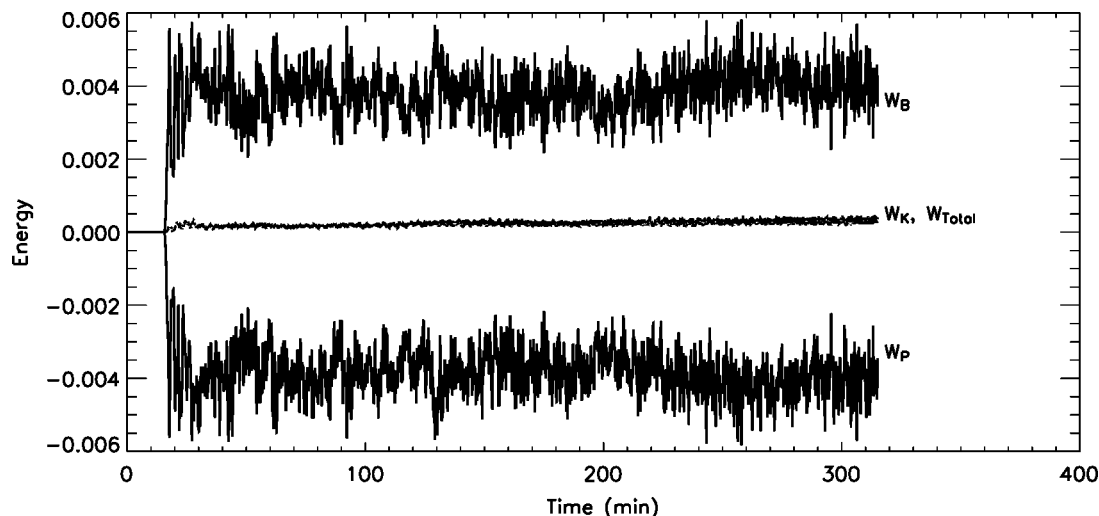


FIG. 10. Time dependence of flux tube averaged magnetic energy  $W_B$ , kinetic energy  $W_K$ , plasma anisotropy energy for firehose mode,  $W_P$ , and the total energy  $W_{\text{total}}$  in energy conservation equation in the nonlinear firehose simulation for the strong turbulence. The energy  $W_V$  due to hyperviscosity is not plotted because of extreme smallness.

Sigsbee *et al.*<sup>7</sup> and Lui and Najimi.<sup>14</sup> The scalograms of the Pi-2 oscillations show a distinctive downward shift of the frequency during the high-amplitude periods. This behavior is also seen in the simulations presented here. Lui and Najimi interpreted the decrease in the frequency of the magnetic oscillations as a nonlinear cascade. The nonlinearity of our model is the origin of the downward frequency shifts in the simulations, perhaps consistent with the characterization in Ref. 14.

### VIII. CONCLUSIONS

We conclude that the correlation between bursty bulk flows and the strong, irregular magnetic fluctuations can be naturally explained in terms of the turbulence generated by the kinetically modified firehose instability. The oscillations would be expected on flux tubes that are shortening in length a few minutes before the arrival of the main dipolarization front. We have shown in detail how the energy transfer takes place and provided the characteristics for the turbulent electric and magnetic fields, both in the high- $\beta$  equatorial region where the waves are generated and also earthward along the flux tube into the low- $\beta$  inner magnetosphere, where the fluctuations are Alfvén waves at high  $k_{\parallel}$ . Remaining tasks are to include kinetic wave-particle interactions, a more detailed equilibrium geometry,<sup>15,16</sup> and more detailed boundary conditions for the partial reflection and absorption of the Alfvénic Poynting flux by the ionosphere.

Earlier discussions of this investigation have also been reported by Horton *et al.*<sup>17,18</sup>

### ACKNOWLEDGMENTS

The authors gratefully acknowledge useful conversations with Sho Ji and Richard Wolf during the course of this work. This work was supported by National Science Foundation under Grant No. ATM-0229863 and the U. S. Department of Energy under Grant No. DE-FG02-04ER54742.

<sup>1</sup>C. X. Chen and R. A. Wolf, *J. Geophys. Res.* **104**, 14613 (1999).

<sup>2</sup>S. Ji and R. A. Wolf, *J. Geophys. Res.* **108**, 1191 (2003).

<sup>3</sup>S. Ji and R. A. Wolf, *J. Geophys. Res.* **30**, 2242 (2003).

<sup>4</sup>G. F. Chew, M. Goldberger, and F. Low, *Proc. R. Soc. London* **A236**, 112 (1956).

<sup>5</sup>L. Kepko and M. Kivelson, *J. Geophys. Res.*, [Space Phys.] **104**, 021 (1999).

<sup>6</sup>L. Kepko and M. Kivelson, *J. Geophys. Res.*, [Space Phys.] **6**, 1903 (2001).

<sup>7</sup>K. Sigsbee *et al.*, *J. Geophys. Res.*, [Space Phys.] **107**(A7), 114 (2002).

<sup>8</sup>T. H. Stix, *Waves in Plasmas* (American Institute of Physics, New York, 1992).

<sup>9</sup>S. P. Gary, *Theory of Space Plasma Microinstabilities* (Cambridge University Press, Cambridge, 1993).

<sup>10</sup>J. D. Huba, N. T. Gladd, and K. Papadopoulos, *Geophys. Res. Lett.* **4**, 125 (1977).

<sup>11</sup>J. D. Huba, N. T. Gladd, and K. Papadopoulos, *Geophys. Res. Lett.* **83**, 5217 (1978).

<sup>12</sup>A. A. Chan, M. Xia, and L. Chen, *J. Geophys. Res.* **99**, 17351 (1994).

<sup>13</sup>R. L. Kaufmann *et al.*, *Pressure Anisotropy and  $B_y$  in the Magnetotail Current Sheet* (American Geophysical Union, Geophys. Monograph, Washington, D.C., 2000), p. 118.

<sup>14</sup>A. T. Y. Lui and A. H. Najimi, *Geophys. Res. Lett.* **24**, 3157 (1997).

<sup>15</sup>W. Horton *et al.*, *J. Geophys. Res.* **98**, 17 (1993); **98**, 327 (1993).

<sup>16</sup>F. Cao and L. C. Lee, *Ann. Geophys.* **12**, 286 (1994).

<sup>17</sup>W. Horton, B. Xu, and H. V. Wong, *Geophys. Res. Lett.* **31**, L06807 (2004).

<sup>18</sup>W. Horton, B. Xu, H. V. Wong, and J. W. V. Dam, *J. Geophys. Res.* **109**, A09216 (2004).